Composite Block Polymer—Microfabricated Silicon Nanoporous Membrane

Eric E. Nuxoll,[†] Marc A. Hillmyer,[‡] Ruifang Wang,[§] C. Leighton,[§] and Ronald A. Siegel*[,†,‖]

Departments of Pharmaceutics, Chemistry, Chemical Engineering & Materials Science, and Biomedical Engineering, University of Minnesota, Minneapolis, Minnesota 55455

ABSTRACT Block polymers offer an attractive route to densely packed, monodisperse nanoscale pores. However, their fragility as thin films complicates their use as membranes. By integrating a block polymer film with a thin (100 μm) silicon substrate, we have developed a composite membrane providing both nanoscale size exclusion and fast transport of small molecules. Here we describe the fabrication of this membrane, evaluate its mechanical integrity, and demonstrate its transport properties for model solutes of large and small molecular weight. The ability to block large molecules without hindering smaller ones, coupled with the potential for surface modification of the polymer and the microelectromechanical system style of support, makes this composite membrane an attractive candidate for interfacing implantable sensing and drug-delivery devices with biological hosts.

KEYWORDS: microelectromechanical system • nanoporous • membrane • block polymer • size selectivity

INTRODUCTION

Nanoporous membranes have long played a role in the industrialized world. Pore sizes and morphologies in such membranes often exhibit significant dispersion, and increasingly stringent demands on pore size, monodispersity, transport resistance, durability, chemical and biological compatibility, processability, and cost have spurred the development of thin membranes with straight, monodisperse nanopores. Contemporary examples include anodized alumina membranes containing straight, densely packed pores as narrow as 5 nm in diameter, and track-etched polymer membranes with pores also less than 10 nm across but with limited pore densities. Pores of either material can be narrowed or functionalized by coating the walls (1−4).

New materials and processes are being developed to provide alternatives to these conventional films. Aligned carbon nanotubes have been used to form pores with interior diameters as small as 2 nm and smooth walls (5, 6). Striemer et al. (7) relied on the volume change during amorphous silicon annealing to create thin, rugged poly(silicon) membranes with maximum pore sizes of less than 17 nm. Desai et al. (8−10) fabricated silicon membranes with arrayed monodisperse pores as small as 7 nm across and demonstrated immunoisolation and cell support. None of these membranes have porosities much above 1%, however. Higher porosities have been achieved by variations around the anodized alumina theme, either by substituting tantalum for aluminum (11) or by transferring the nanoporous pattern from alumina onto a silicon nitride substrate (12). The Si_3N_4 membranes were integrated into a microfluidic device supporting neuronal cells. These membranes share the high porosity of alumina but also many of its drawbacks.

Block polymers offer another strategy for nanoporous membrane development (13−15). With proper choice of monomers and block lengths, these materials self-assemble into uniform cylinders of the minority component embedded in the majority component. Under proper conditions, the cylinders align perpendicularly to the plane of a thin film (16−19). Selective removal of the minority block yields films with straight, monodisperse, densely packed pores with diameters down to about 10 nm. Size selectivity of such nanoporous films has been demonstrated electrochemically (20), and they have been used to template nanoscale features in other materials (21−24). These films, however, are typically too thin and fragile to serve as standalone membranes. Mechanical properties are improved with thicker nanoporous membranes at the expense of higher transport resistance (25−28). For example, Yang et al. (29, 30) transferred a poly(styrene)−poly(methylmethacrylate) (PS−PMMA) film onto 150-μm-thick porous poly(sulfone), etched the PMMA component, and used this assembly to filter viruses, but this support structure also greatly decreased the membrane's permeability.

To support a nanoporous polymer film with minimal increase in the transport resistance, we prepared a composite nanoporous membrane system, integrating a poly(styrene)−poly(isoprene)−poly(lactide) (PS−PI−PLA) triblock polymer (31, 32) derived membrane with a microfabricated silicon support containing wide, short, straight, and densely packed pores. Here we describe this integrated fabrication, evaluate the viability of the supported nanoporous mem-
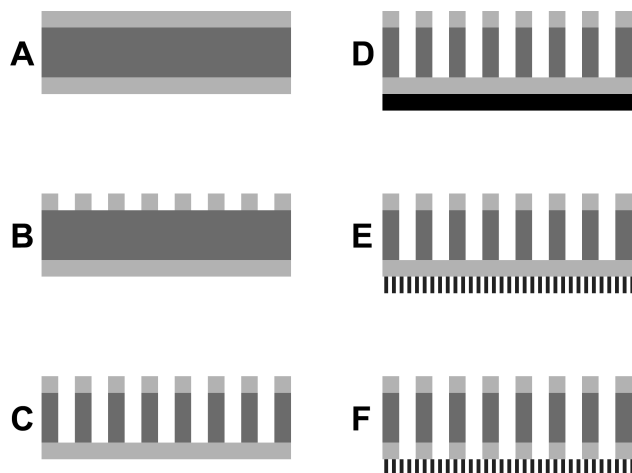
FIGURE 1. Fabrication scheme for a composite nanoporous membrane. The silicon wafer (dark gray, 100 μm thick) is coated on both sides with low-stress silicon nitride (light gray, 40 nm) (A). Si_3N_4 is patterned via photolithography and RIE (B). Pores are anisotropically dry-etched through silicon (C). The triblock copolymer (black, 80 nm) is spin-coated onto top-side Si_3N_4 and annealed (D). PLA polymer domains are selectively removed by NaOH etching, followed by a brief oxygen RIE (E) Si_3N_4 covering silicon pores is removed by HF etching (F). Note that the figures are not drawn to scale.

brane under various mechanical challenges, and demonstrate its size-based transport selectivity.

Membrane Fabrication. Figure 1 shows the fabrication scheme for the composite membrane. A 100-μm-thick double-side-polished silicon wafer is coated on both sides with 40 nm of low-stress silicon nitride (Si_3N_4) by low-pressure chemical vapor deposition (A). The top side of the wafer is coated with photoresist and patterned with a dark-field mask containing numerous 50 × 50 arrays of 20 μm squares spaced 20 μm apart. Following development, the wafer is glued onto a 500-μm-thick handle wafer using photoresist. The wafer stack is hard-baked and subjected to reactive ion etching (RIE) to remove the exposed top-side Si_3N_4 squares (B). Bosch process-directed RIE (DRIE) anisotropically etches these squares through the silicon wafer with an etch rate of ≈2 μm/min. The etched wafer is removed from its handle and cleaned by oxygen RIE. The resulting microporous support is 25% porous, with straight, nearly square pores 100 μm long, each capped on the bottom by the remaining 40 nm layer of Si_3N_4 (C). Figure 2 shows optical top, cross-sectional, and bottom views of the microporous support.

To prepare the nanoporous skin, the Si_3N_4 surface of the support is immersed in a 5% solution of (dichloromethyl)-octylsilane in toluene, coating the surface with covalently bonded alkyl chains (33) to promote polymer adhesion to the Si_3N_4 surface. A chlorobenzene solution of PS−PI−PLA (M_n = 69.5 kg/mol; 56% PS, 10% PI, 34% PLA by weight; polydispersity index = 1.14; see refs 28 and 29) is then spin-coated onto the support. PI-sheathed PLA domains spontaneously self-assemble into discrete cylinders aligned perpendicularly to the film surface within a continuous planar PS phase (31, 34−36) (Figure 1D). The composite device is submerged in 0.05 M NaOH in a 60%/40% (v/v) water−methanol solution for 45 min, selectively removing most of the
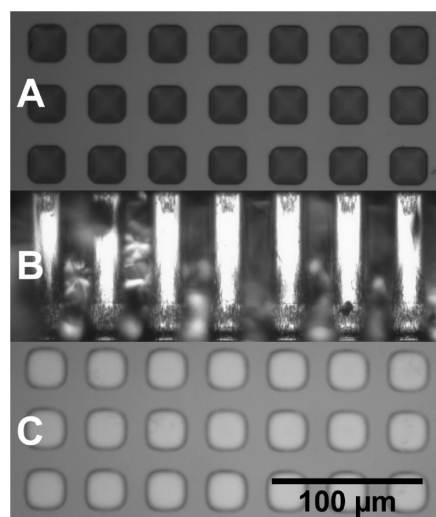

FIGURE 2. Microporous silicon support as viewed from the top (A), cross section (B), and bottom (C).
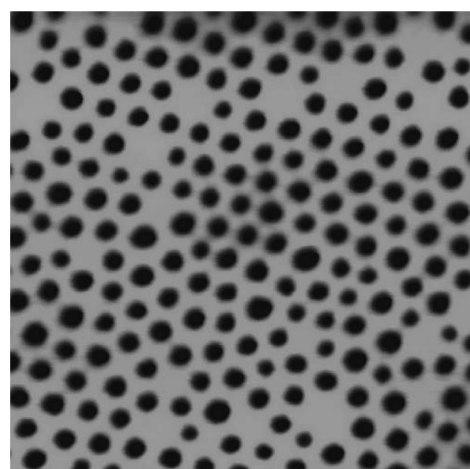

FIGURE 3. Tapping-mode AFM height image of a nanoporous block polymer film on Si_3N_4. Pore diameters are 43 nm ± 11% RSD. The image is 1 μm square.

PLA and forming nanoscale PI-lined pores in the PS continuum (Figure 1E). Pores at this stage are imaged in Figure 3 by tapping-mode atomic force microscopy (AFM) and are found to have mean pore sizes of 43 nm ± 11% relative standard deviation (RSD). The film thickness was determined by AFM to be 82 nm. A total of 10 s of low-power oxygen RIE removes any polymer remaining at the bottom of the pores in the nanoporous PS−PI film (23).

To remove Si_3N_4 between the micropores and the nanoporous block polymer film, a 30 μL drop of 49% hydrofluoric acid (HF) is introduced on the silicon side of the device (Figure 1F). While HF may affect the PI sheaths, the PS film is largely unaffected by exposure to HF (37, 38).

Alignment Testing and Pore Continuity. To confirm the perpendicular domain alignment suggested by Figure 3, devices at the stage depicted in Figure 1E were subjected to an RIE protocol that etches Si_3N_4 as well as the polymer, transferring the polymer's nanopores into the underlying Si_3N_4. The remaining polymer was removed by both oxygen RIE and/or a piranha bath (4:1 concentrated H_2SO_4−30% H_2O_2). Figure 4 (scanning electron microscopy,
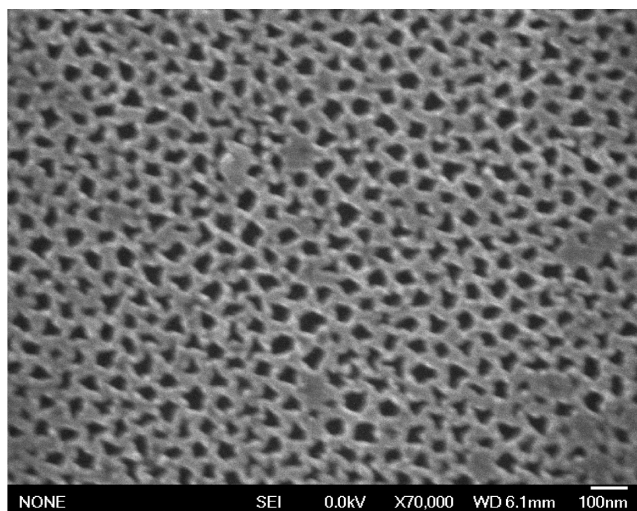
FIGURE 4. Demonstration of pore alignment in a nanoporous block polymer film. The film was used as a mask to etch the pits shown in this SEM image. The irregular pit shapes are likely due to product deposition during the etch.
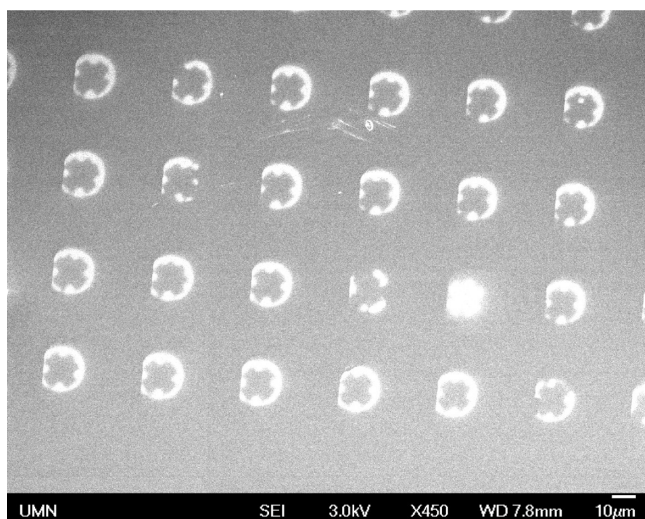

FIGURE 5. SEM image of permalloy (light) on a silicon substrate (dark) following epitaxy using the nanoporous membrane as a mask. The feature size and spacing match those of the membrane's microporous support. The cross-shaped pattern in each feature corresponds to the topography of the nanoporous polymer film. The bright feature in the lower-right quadrant shows growth under a micropore lacking a nanoporous polymer cover.

SEM) shows that the pore pattern from the polymer is transferred into the nitride by etching, consistent with perpendicular alignment of pores in the film. The irregular shapes of the etched domains are likely the result of fluoropolymer deposition on the PS film during RIE.

To confirm that the nanopores span the entire block polymer film, finished devices as depicted in Figure 1F were used as masks for molecular beam deposition of permalloy ($Ni_{80}Fe_{20}$) onto a silicon wafer. Prior to deposition, different portions of the membrane were subjected to various oxygen RIE times, ranging from 0 to 25 s. During deposition, 20 nm of permalloy was grown on the substrate at a rate of 0.2 Å/s, and the substrate was subsequently inspected by SEM. Figure 5 shows the permalloy deposition pattern in the absence of oxygen RIE. Under each micropore, bright per-
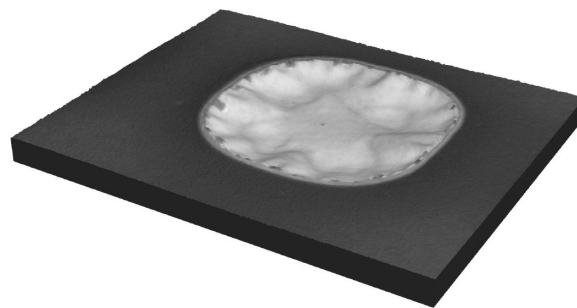

FIGURE 6. Confocal microscope topograph of a polymer film spanning a 20 μm pore in the silicon support. The z axis is magnified by a factor of 5 to better view the curvature in these pore coverings.

malloy-coated regions surround a dark cross-shaped pattern. This pattern, as will be seen below, correlates with the topography of the polymer and probably reflects wrinkling and dealignment of nanopores with the direction of the permalloy beam. Confocal microscopy conducted before and after permalloy deposition confirmed that the polymer film covered the pores throughout the process. (One micropore in Figure 5 appears to have lost its block polymer film cover, explaining the complete permalloy coverage of the silicon substrate below it.)

Because permalloy grew under the block polymer film with no oxygen RIE, this etching step may not be required to provide pores that span the film. Exposure to oxygen RIE over increasing times tended to erode the block polymer layer. Therefore, RIE may be regarded as a "polishing" step, which should not be overutilized.

Imaging and Mechanical Evaluation of the Nanoporous Membrane. The result of the fabrication steps is a two-layer composite (asymmetric) membrane with both microscale and nanoscale pores. As a free-standing membrane, the nanoporous polymer is too thin and fragile for most applications. The underlying microporous silicon membrane provides mechanical support to the film. Morphology and viability of the film, attached to the microporous support, were investigated by a variety of means.

Figure 6 shows a reflectance confocal image of an intact film spanning a 20 μm pore. The film exhibits shallow wavelike wrinkles ($\sim$200 nm peak to trough) intersecting at the pore center. Wrinkles correlate with the pattern seen in the permalloy growth of Figure 5 suggesting, as was already noted, that line-of-sight transmittance of the molecular beam was altered by the local angle of the film. Prior to spin coating, the thin layer of Si_3N_4 (40 nm) over the pores was also wavy, probably a consequence of the tensile stress present in the Si_3N_4 film. The overlying polymer layer maintained this shape after the nitride was removed. Thicker (90 nm) Si_3N_4 films provide much flatter pore coverings.

Stress is expected to be most concentrated near micropore perimeters. To determine whether stress leads to mechanical failure at the perimeter, a "lift and shift" procedure was used, enabling visualization of patches of membrane covering the micropores. The wrinkle patterns provided visible markers designating these patches. In this case, the composite membrane was formed without surface treatment of Si_3N_4, resulting in reduced adhesion between
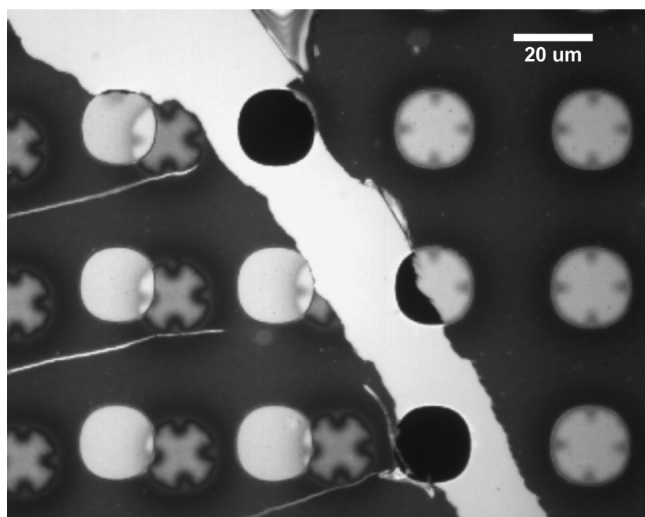
FIGURE 7. Optical micrograph of a nanoporous block copolymer on a microporous silicon support. The polymer on the left was lifted and moved ~30 μm to the left, allowing the polymer to be scrutinized independently from the pore it had previously covered. The exposed region of the microporous support is bright-colored and runs from the upper left to the lower right. Black uncovered pores are visible in this region. Covered pores are brightly colored; the ones on the right have their original "wavy" pore coverings. On the left, the original pore coverings are visible as light-colored X's partially overlaying the next column of pores to their left. Small tears are also visible as bright lines running laterally from the left-hand edge.

the nitride and the polymer film. Upon careful immersion in water, a section of the polymer film delaminated from the support. Slight lateral translation of the support caused the delaminated polymer to tear away from the adhered polymer. Lifting the support and carefully wicking away the water, the delaminated polymer laid back onto the support, approximately 30 μm to the left of its original position. This delaminated polymer and adhered polymer are seen respectively at the left and right sides of Figure 7, with a bright stripe of newly exposed nitride in between.

In Figure 7, shifted patches of the film that previously covered the micropores are identified by cross-shaped patterns, now overlapping micropores one column to the left. The crosses correlate with both the confocal topography in Figure 6 and the permalloy deposition patterns in Figure 5. There is no evidence of fracture inside the patches, and the three horizontal tears from the left edge of the figure do not propagate around or into the patch perimeters as one might expect if the perimeters were particularly weak.

In another test of the system's robustness, we altered the fabrication protocol to precipitate a solid on the film. Rather than using aqueous HF to remove the Si_3N_4 covering the support pores (per Figure 1E), we used gaseous HF. Aqueous HF provides a medium through which the reaction products (specifically NH_4F) diffuse away. Because gas-phase etching offers no exit route for NH_4F, salt crystals precipitate on the nanoporous polymer film, as shown in Figure 8. Some of these crystals are apparently supported by the polymer film, which conforms to the crystals, as shown in the confocal topograph in Figure 8A. The topography persists after dissolution of the crystals in excess deionized water. Figure 8B, an AFM relief map, shows a similar crystal-induced promi-
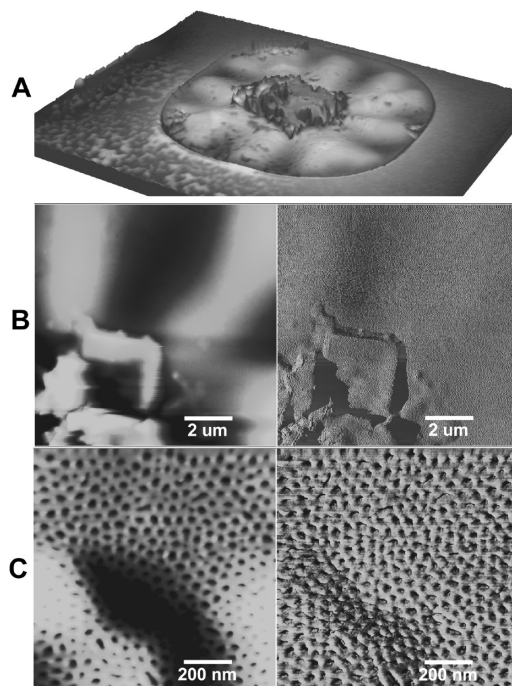

FIGURE 8. (A) Confocal microscopy topograph of a polymer pore covering subjected to the precipitation of Si_3N_4 etch products. (B) Tapping-mode AFM image (height on the left and phase on the right) of a pore from the same sample as that on top. (C) AFM image of the center 1 μm from the middle image, showing the edge of the precipitation zone. The polymer retains its nanoporous morphology over these contours and appears undamaged.

nence along with radial wrinkles. At higher magnification (Figure 8c), the nanoscale pore structure of the polymer is seen to be unaffected by the local topography, even along high-relief contours.

Considering these observations, we conclude that the polymer film covering the micropores withstands localized stress and deformation without either tearing or losing its nanoporous morphology. The immersions and shear suffered by the samples during this investigation far exceed the physical challenges they would likely receive in most diffusional transport systems.

Transport Studies. Transport resistance and size selectivity of the bilayered composite were evaluated in a side-by-side diffusion cell (Crown Glass, 3 mL on both sides, with a 9 mm orifice). A (2 mm)^2 composite, embedded in the original wafer, was mounted and clamped between the donor and receptor cells with the block polymer film facing the receptor cell. Methyl orange (MO; Sigma, MW = 327 g/mol) and dextran blue (DEX; Sigma, MW = 2 × 10^6 g/mol) were introduced into the donor cell, and their time-dependent concentration in the receptor cell was monitored by UV/vis spectroscopy. As shown in Figure 9A, the cumulative flux of MO increased nearly linearly with time, with almost 15% of the molecules crossing the composite membrane during the first 48 h. DEX was effectively blocked, however, with less than 1% crossing the composite over 6 weeks, showing a 1500-fold lower permeability.

As a control, the composite membrane was replaced by a commercial anodized alumina membrane (Anodisc, Whatman), 60 μm thick and with a nominal pore size of 200 nm.
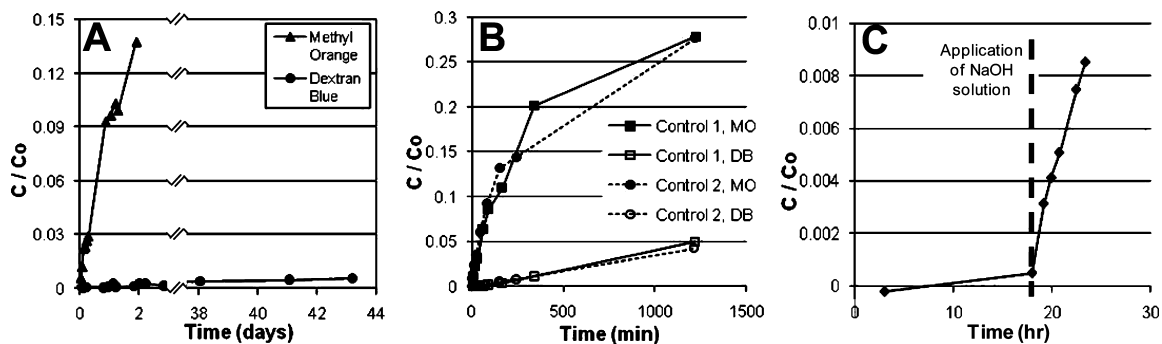
FIGURE 9. Membrane breakthrough curves. (A) MO and DEX across a nanoporous composite membrane, indicating a 1500-fold permeability difference between MO and DEX. (B) MO and DEX across an Anodisc control membrane, indicating a 30-fold permeability difference between MO and DEX. (C) MO across a composite membrane without prior PLA block removal. NaOH was added after 18 h, prompting a dramatic increase in permeability. The magnitude of the small negative value reported at the earliest point is below the noise limit of the UV/Vis detector.

Because the lateral dimension of these pores well exceeds the hydrodynamic radii of either solute, differences in transport are mostly attributable to differences in aqueous diffusivities of MO and DEX inside the pores. As shown in Figure 9B, DEX transport across this nonselective membrane is only 30-fold lower than MO transport, as expected from its much larger hydrodynamic radius. The composite membrane, with nanopore diameters of ~43 nm, therefore demonstrates a ~50-fold increase in selectivity compared to that of Anodisc, because of the size exclusion of DEX and enhanced hydrodynamic interactions between DEX and the nanopore walls.

It should be noted that the Anodisc membrane was uniformly porous, and its area supporting transport was much larger (~16×) than that of the bilayer composite. Hence, fluxes were much higher, necessitating more frequent sampling. In ultimate practice, the pore coverage in the bilayer composite could be increased to the same order as that of Anodisc, and comparable MO fluxes with enhanced selectivity versus DEX should be observed. Also, while qualitative changes in size selectivity between the composite membrane and Anodisc are obvious, the extremely low fluxes of DEX preclude precise quantitation. Both membranes are very thin, and unstirred layers may play a significant role in determining the flux, particularly for MO. Calculations (see the Supporting Information), based on the flux of MO through Anodisc and the aqueous diffusion coefficient of MO, suggest boundary layers on the order of 200 μm, thicker than either membrane. Because these effects should be more significant for MO than for DEX, the difference in selectivity between the two membranes may be greater than what was inferred from the slopes of the curves in Figure 9A,B.

In another experiment, a composite membrane was prepared without the PLA removal step and mounted in the diffusion cell. No MO diffused across the membrane for 18 h, indicating that all three components of the block polymer membrane are impermeable. The downstream cell was then spiked with 0.5 mL of 0.37 M NaOH to degrade the PLA block. MO transport was soon observed downstream, as shown in Figure 9C. No DEX was detected in the receptor cell, however, even after 5 days of extreme upstream DEX

concentration. As shown in Figure 9C, the normalized MO flux for the initially plugged membrane was about half that seen in Figure 9A, possibly because of subtle differences in cell hydrodynamics or incomplete removal of material from the pore regions (there was no oxygen etch step). These results suggest that PLA domains span the entire block polymer film and demonstrate that size-selective transport through this membrane can be activated with a simple chemical signal.

DISCUSSION AND CONCLUSIONS

We have demonstrated fabrication and viability of a composite membrane combining the self-assembled nanoporous morphology of block polymers with the strength and regularity of micromachined silicon. This composite nanoporous membrane should be sufficiently robust for a variety of membrane applications, and the microfabricated membrane support should be amenable to scale-up and integration in microelectromechanical system devices.

Transport studies demonstrated minimal resistance of the membrane to small-molecule transport and high resistance to transport of large macromolecules. This combination of large permeability and large size selectivity may be valuable in a variety of applications such as biomedical sensors and controlled delivery systems.

We have also demonstrated the ability to chemically trigger transport through the membrane, effectively turning the membrane into a controlled release device. This trigger may be tunable by a variety of strategies such as incorporating comonomers (e.g., glycolide) in the PLA block, assuming they do not significantly impact the polymer morphology. Alternatively, following etching of PLA, one may consider using the PI nanopore lining as a locus for functionalization with polymers that passivate the structure or mediate transport selectivity, perhaps in a stimuli-sensitive manner (32). Similarly, the PI lining can be used to anchor bioactive agents such as enzymes and antibodies.

Finally, by modification of the chain lengths in the block polymer, the size of the nanoscale pores can be tuned. The silicon support can also be optimized. We have already built supports with pore spacings as thin as 5 μm, and thinner

wafers (already commercially available) should make that process even easier.

Supporting Information Available: Fabrication details, pattern transfer into silicon nitride, UV/vis calibration/detection limits, diaphragm cell experiments, calculation of boundary layers, and instrumentation. This material is available free of charge via the Internet at http://pubs.acs.org.

REFERENCES AND NOTES

(1) Martin, C. R. *Science* **1994**, *266*, 1961.
(2) Jirage, K. B.; Hulteen, J. C.; Martin, C. R. *Science* **1997**, *278*, 655.
(3) Lee, S. B.; Martin, C. R. *Chem. Mater.* **2001**, *13*, 3236.
(4) Yamaguchi, A.; Uejo, F.; Yoda, T.; Uchida, T.; Tanamura, Y.; Yamashita, T.; Teramae, N. *Nat. Mater.* **2004**, *3*, 337.
(5) Hinds, B. J.; Chopra, N.; Rantell, T.; Andrews, R.; Gavalas, V.; Bachas, L. G. *Science* **2004**, *303*, 62.
(6) Holt, J. K.; Park, H. G.; Wang, Y.; Stadermann, M.; Artyukhin, A. B.; Grigoropoulos, C. P.; Noy, A.; Bakajin, O. *Science* **2006**, *312*, 1034.
(7) Striemer, C. C.; Gaborski, T. R.; McGrath, J. L.; Fauchet, P. M. *Nature* **2007**, *445*, 749.
(8) Leoni, L.; Boiarski, A.; Desai, T. A. *Biomed. Microdevices* **2002**, *4*, 131.
(9) Desai, T. A.; West, T.; Cohen, M.; Boiarski, A.; Rampersaud, A. *Adv. Drug Delivery Rev.* **2004**, *56*, 1661.
(10) Lopez, C. A.; Fleischman, A. J.; Roy, S.; Desai, T. A. *Biomaterials* **2006**, *27*, 3075.
(11) Singh, S.; Greiner, M. T.; Kruse, P. *Nano Lett.* **2007**, *9*, 2676.
(12) Wolfrum, B.; Mourzina, Y.; Sommerhage, F.; Offenhäusser, A. *Nano Lett.* **2006**, *6*, 453.
(13) Hawker, C. J.; Russell, T. P. *MRS Bull.* **2005**, *30*, 952.
(14) Shin, K.; Leach, K. A.; Goldbach, J. T.; Kim, D. H.; Jho, J. Y.; Tuominen, M.; Hawker, C. J.; Russell, T. P. *Nano Lett.* **2002**, *2*, 933.
(15) Bang, J.; Kim, S. H.; Drockenmuller, E.; Misner, M. J.; Russell, T. P.; Hawker, C. J. *J. Am. Chem. Soc.* **2006**, *128*, 7622.
(16) Kim, S. H.; Misner, M. J.; Xu, T.; Kimura, M.; Russell, T. P. *Adv. Mater.* **2004**, *16*, 226.
(17) Cavicchi, K. A.; Russell, T. P. *Macromolecules* **2007**, *40*, 1181.
(18) Xiang, H.; Lin, Y.; Russell, T. P. *Macromolecules* **2004**, *37*, 5358.
(19) Xu, T.; Zvelindovsky, A. V.; Sevink, G. J. A.; Lyakhova, K. S.; Jinnai, H.; Russell, T. P. *Macromolecules* **2005**, *38*, 10788.
(20) Li, Y.; Ito, T. *Anal. Chem.* **2009**, *81*, 851.
(21) Hillmyer, M. A. *Adv. Polym. Sci.* **2005**, *190*, 137.
(22) Black, C. T.; Ruiz, R.; Breyta, G.; Cheng, J. Y.; Colburn, M. E.; Guarini, K. W.; Kim, H.-C.; Zhang, Y. *IBM J. Res. Dev.* **2007**, *51*, 605.
(23) Kubo, T.; Parker, J. S.; Hillmyer, M. A.; Leighton, C. *Appl. Phys. Lett.* **2007**, *90*, 233113.
(24) Black, C. T.; Guarini, K. W.; Breyta, G.; Colburn, M. C.; Ruiz, R.; Sandstrom, R. L.; Sikorski, E. M.; Zhang, Y. *J. Vac. Sci. Technol. B* **2006**, *24*, 3188.
(25) Liu, G.; Ding, J.; Stewart, S. *Angew. Chem., Int. Ed.* **1999**, *38*, 835.
(26) Liu, G.; Ding, J.; Hashimoto, T.; Kimishima, K.; Winnik, F. M.; Nigam, S. *Chem. Mater.* **1999**, *11*, 2233.
(27) Cooney, D. T.; Hillmyer, M. A.; Cussler, E. L.; Moggridge, G. D. *Crystallogr. Rev.* **2006**, *12*, 13.
(28) Phillip, W. A.; Rzayev, J.; Hillmyer, M. A.; Cussler, E. L. *J. Membr. Sci.* **2006**, *286*, 144.
(29) Yang, S. Y.; Ryu, I.; Kim, H. Y.; Kim, J. K.; Jang, S. K.; Russell, T. P. *Adv. Mater.* **2006**, *18*, 709.
(30) Yang, S. Y.; Park, J.; Yoon, J.; Ree, M.; Jang, S. K.; Kim, J. K. *Adv. Funct. Mater.* **2008**, *18*, 1371.
(31) Guo, S.; Rzayev, J.; Bailey, T. S.; Zalusky, A. S.; Olayo-Valles, R.; Hillmyer, M. A. *Chem. Mater.* **2006**, *18*, 1719.
(32) Bailey, T. S.; Rzayev, J.; Hillmyer, M. A. *Macromolecules* **2006**, *39*, 8772.
(33) Fadeev, A. Y.; McCarthy, T. J. *Langmuir* **2000**, *16*, 7268.
(34) Kubo, T.; Wang, R. F.; Olson, D. A.; Rodwogin, M.; Hillmyer, M. A.; Leighton, C. *Appl. Phys. Lett.* **2008**, *93*, 133112.
(35) Olayo-Valles, R.; Guo, S.; Lund, M. S.; Leighton, C.; Hillmyer, M. A. *Macromolecules* **2005**, *38*, 10101.
(36) Park, C.; Cheng, J. Y.; Fasolka, M. J.; Mayes, A. M.; Ross, C. A.; Thomas, E. L.; De Rosa, C. *Appl. Phys. Lett.* **2001**, *79*, 848.
(37) Mao, H.; Hillmyer, M. A. *Macromolecules* **2005**, *38*, 4038.
(38) Mao, H. Ph.D. Thesis, University of Minnesota, Minneapolis, MN, 2006.
(39) Sigma did not provide a hydrodynamic radius; GE Healthcare lists a stokes radius of 27 nm for its 2 MDa dextran blue.

AM900013V